ACS NANO

www.acsnano.org

ARTICLE

Enhancing Proton Co-Intercalation in Iron Ion Batteries Cathodes for Increased Capacity

Ze He, Gao Wang, Ruohan Yu, Yalong Jiang, Meng Huang, Fangyu Xiong, Shuangshuang Tan, Michael F. L. De Volder,* Qinyou An,* and Liqiang Mai*

Cite This: *ACS Nano* 2024, 18, 17304–17313

Read Online

ACCESS | Metrics & More | Article Recommendations | Supporting Information

ABSTRACT: Recently, aqueous iron ion batteries (AIIBs) using iron metal anodes have gained traction in the battery community as low-cost and sustainable solutions for green energy storage. However, the development of AIIBs is significantly hindered by the limited capacity of existing cathode materials and the poor intercalation kinetic of Fe^{2+}. Herein, we propose a H^+ and Fe^{2+} co-intercalation electrochemistry in AIIBs to boost the capacity and rate capability of cathode materials such as iron hexacyanoferrate (FeHCF) and $Na_4Fe_3(PO_4)_2(P_2O_7)$ (NFPP). This is achieved through an electrochemical activation step during which a FeOOH nanowire layer is formed in situ on the cathode. This layer facilitates H^+ co-intercalation in AIIBs, resulting in a high specific capacity of 151 mAh g^{-1} and 93% capacity retention over 500 cycles for activated FeHCF cathodes. We found that this activation process can also be applied to other cathode chemistries, such as NFPP, where we found that the cathode capacity is doubled as a result of this process. Overall, the proposed H^+/Fe^{2+} co-insertion electrochemistry expands the range of applications for AIBBs, in particular as a sustainable solution for storing renewable energy.

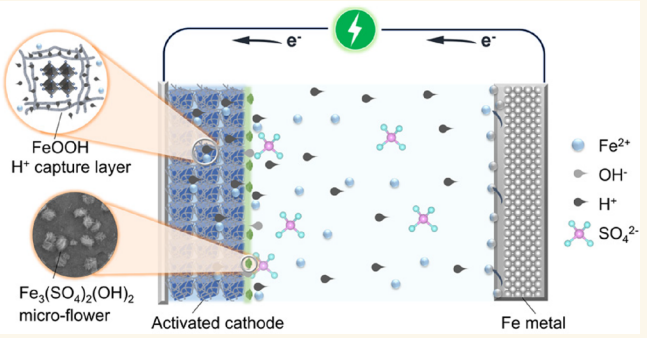

KEYWORDS: *iron ion battery, cathode materials, electrochemical activation, proton co-intercalation, high capacity*

1. INTRODUCTION

Large-scale energy storage systems (LESSs) are vital for the use of renewable energy such as solar, wind, and tidal generation.[1] While lithium-ion batteries (LIBs) have dominated portable devices and electric vehicles because of their high specific energy and power density,[2] they are flammable and are increasingly becoming more expensive, which make them unlikely to address all LESS needs.[3] Researchers have increasingly directed their focus toward cost-effective and nonflammable aqueous battery systems. Among these, Zn-ion batteries (ZIBs) are widely studied because of the intrinsic merits of Zn metal anode, which features high theoretical capacities (820 mAh g^{-1}, 5854 mAh cm^{-3}), low cost, and low redox potential (−0.76 V vs the standard hydrogen electrode).[4] While the latter allows for relatively high operating voltage compared to other aqueous batteries, it is a double-edged sword as substantial amounts of H_2 evolve on the surface of Zn.[5] Here, we instead focus on Fe-ion batteries using an Fe metal anode. While the redox potential of Fe/Fe^{2+} is approximately 0.3 V higher than that of Zn/Zn^{2+}, this increases the stability of aqueous electrolytes,[6] and importantly, previous reports have demonstrated that Fe does not form dendrites cycling in slightly acidic electrolytes, which is an important advantage over ZIBs.[6] In addition, Fe is the most abundant metal in the earth's crust, the reserves of iron are 560 times that of zinc, the price of iron is 1/43 that of zinc,[7] and its theoretical gravimetric and volumetric capacities (960 mAh g^{-1} and 7557 mAh cm^{-3}) are higher than those of zinc and some emerging anodes such as bismuth.[8,9] These attractive properties have gradually attracted interest from the battery community in Fe ions batteries. Recently, insoluble Prussian blue (IPB),[6] sulfur,[10] iodine,[11] vanadium oxide,[12] $VOPO_4 \cdot 2H_2O$,[13] and cross-linked polyaniline (C-PANI)[14] have been reported as cathode materials for AIIBs. However, due to the high insertion energy barriers, limited specific capacities and rate capabilities can be achieved through Fe^{2+} intercalating/deintercalating. For example, the IPB cathode has been reported to achieve a discharge capacity of 60 mAh g^{-1} at

Received: April 26, 2024
Revised: June 3, 2024
Accepted: June 11, 2024
Published: June 21, 2024

Downloaded via WUHAN UNIV OF TECHNOLOGY on September 6, 2025 at 05:35:39 (UTC).
See https://pubs.acs.org/sharingguidelines for options on how to legitimately share published articles.

ACS Publications

© 2024 American Chemical Society

https://doi.org/10.1021/acsnano.4c05561
ACS Nano 2024, 18, 17304–17313

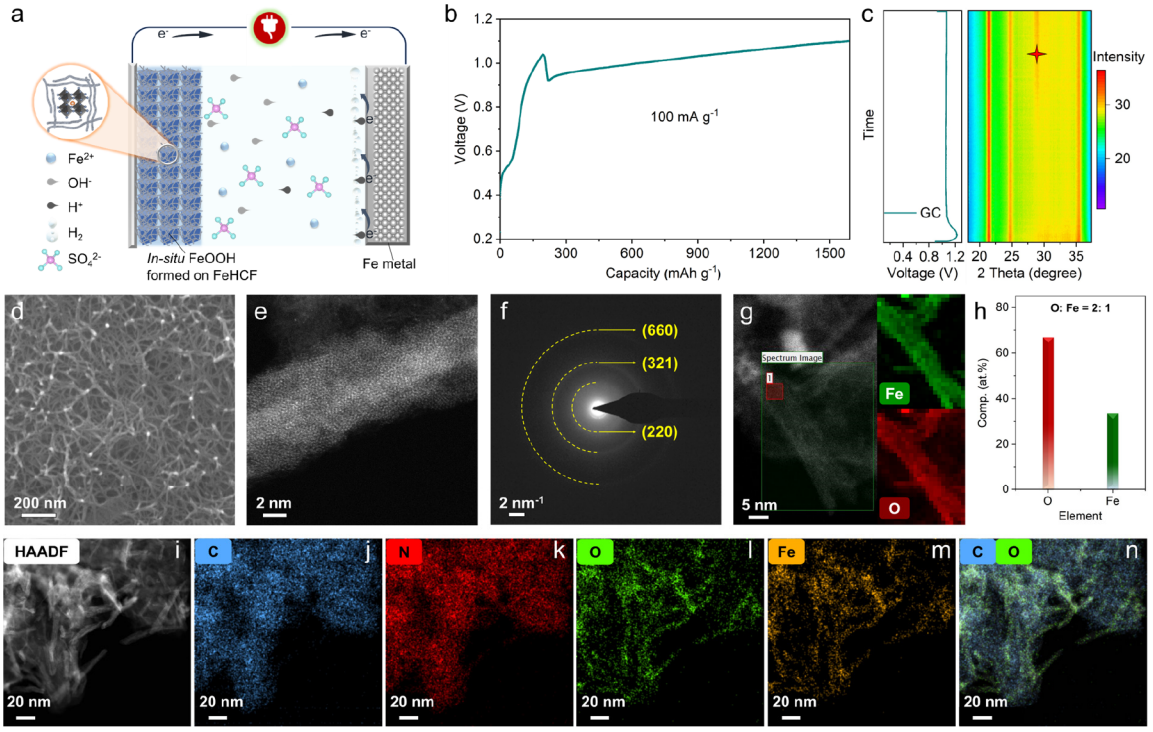

Figure 1. In situ construction of FeOOH layer on FeHCF cathodes during electrochemical activation. (a) Schematic of the electrochemical activation process. (b) Voltage−time curve during electrochemical activating. (c) In situ XRD characterization and the corresponding galvanostatic charge/discharge (GCD) potential profiles during activation process. (d) SEM image of the surface of the activated FeHCF electrode. (e) STEM-HAADF image of the activation product and the corresponding (f) elected area electron diffraction (SAED) image. (g) STEM-EELS elemental mapping of the activation product and the corresponding (h) element ratio. (i−n) EDS-HAADF elemental mappings of the activated FeHCF electrode.

60 mA g^{-1}, which is more than 2 times lower than its theoretical capacity, and limits the practical applications of AIIBs.[6]

Proton co-intercalation has been regarded as a promising method for achieving better electrochemical performance in aqueous battery systems.[15−17] H^+ ions have the lowest weight, smallest ionic radius, and best kinetics of all ions[18−20] and can insert into active sites of host materials where multivalent ions cannot intercalate,[21] leading to improved electrochemical performance.[22,23] H^+ co-insertion has been reported to enhance the capacity,[15,24] cycling stability,[16,17] and rate performance[25,26] in other aqueous batteries based on Na-ion,[27] K-ion,[28] Zn-ion,[29] Al-ion,[30,31] Mg-ion,[32] and NH_4^+-ion,[16] but to the best of our knowledge, this has not been reported for Fe-ion batteries to date.

Herein, we modify an iron hexacyanoferrate (FeHCF) cathode by a simple electrochemical activation process to enable H^+ and Fe^{2+} co-insertion/extraction chemistry. Benefiting from the synergistic effect of H^+/Fe^{2+} co-intercalation, the activated-FeHCF delivers significantly improved capacity, stability, and rate performance in AIIBs. A high capacity of 151 mAh g^{-1} was achieved with this cathode design versus a Fe metal anode. Ex situ scanning transmission electron microscopy (STEM), electron energy loss spectroscopy (EELS), and scanning electron microscopy (SEM) revealed the activation product is FeOOH, which can promote the proton insertion process. In situ X-ray diffraction (XRD), in situ Raman, and ex situ X-ray photoelectron spectroscopy (XPS) confirmed the H^+/Fe^{2+} co-insertion mechanism of activated-FeHCF. Furthermore, the activation process was successfully extended to the $Na_4Fe_3(PO_4)_2(P_2O_7)$ (NFPP) cathode, resulting in a doubled capacity.

2. RESULTS AND DISCUSSION

FeHCF cathode was synthesized using a co-precipitation method of mixing $FeSO_4$ and $K_4Fe(CN)_6$ solutions. The synthesized FeHCF displays a relatively uniform nanoparticle structure with tens of nanometers in diameter (Figures S1 and S2). High-resolution transmission electron microscopy (HRTEM) and XRD results confirm the face-centered cubic structure (Figures S3 and S4). The Fourier transform infrared (FT-IR) spectra reveals the metal−organic compound structure[33] (Figure S5). Fe/FeHCF batteries were assembled using the FeHCF cathode, 0.5 M $FeSO_4$ electrolyte, and an Fe foil anode. Overcharging was carried out for 16 h in the first cycle (activation process), leading to the in situ construction of a FeOOH layer onto the FeHCF electrode, as illustrated in Figure 1a. During the overcharging process, the hydrogen evolution reaction (HER) occurs at the iron metal anode, while OH^- ions migrate to the cathode side and react with Fe^{2+} ions to form $Fe(OH)_2$ (eq 1). Subsequently, $Fe(OH)_2$ further undergoes oxidation, resulting in the formation of FeOOH on the FeHCF electrode (eq 2). This activation process can be represented by the following equations:

$$Fe^{2+} + 2OH^- \rightarrow Fe(OH)_2 \quad (1)$$

$$Fe(OH)_2 + OH^- - e^- \rightarrow FeOOH + H_2O \quad (2)$$

In the galvanostatic charge−discharge (GCD) curve of the activation process, a sudden voltage decrease is observed when the voltage reaches 1.04 V, indicating that FeOOH has crossed

https://doi.org/10.1021/acsnano.4c05561
ACS Nano 2024, 18, 17304−17313

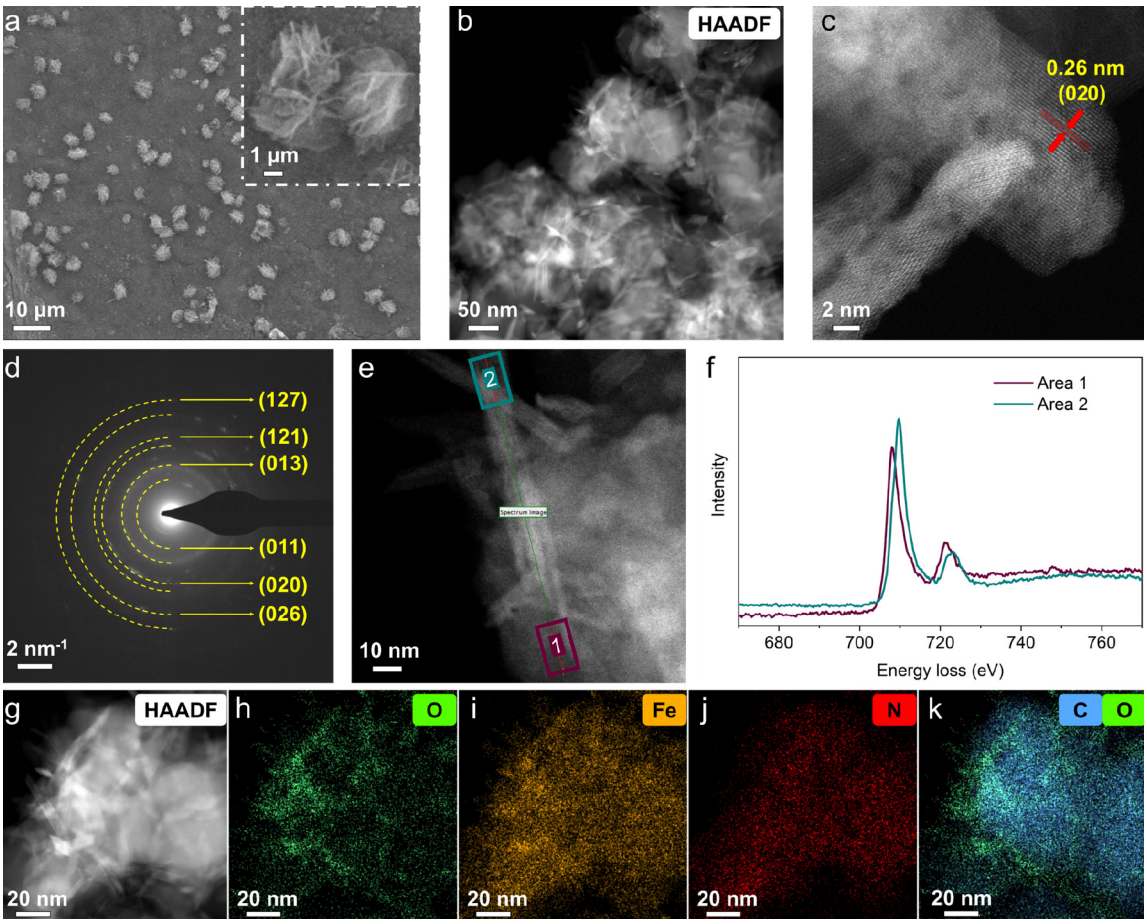

Figure 2. Proton intercalation in activated FeHCF cathodes. (a) SEM image of the surface of the activated FeHCF electrode after discharge, with inset showing the high-magnified image. (b) STEM-HAADF image of the discharge product. (c) High-resolution STEM-HAADF image of microflower and the corresponding (d) SAED image. (e) STEM image of the activated FeHCF electrode after 50 cycles at the discharge state and (f) the corresponding STEM-EELS data collected from area 1 and area 2. (g–k) EDS-HAADF elemental mappings of the activated FeHCF particles after electrochemical cycling.

the nucleation barrier and commenced its formation on the FeHCF electrode (Figure 1b). In situ XRD characterization (Figure 1c) shows the gradual formation of FeOOH during the activation process. The diffraction peaks at 24.75° and 35.36° are identified as the (220) and (440) planes of FeHCF,[34] while the peak at 21.5° belongs to the cling film window. During activation, the diffraction peaks of FeHCF remained unchanged, indicating that FeHCF did not participate in the activation process. After the sudden voltage decrease, an additional peak at 28° gradually appeared during the further activation, which can be identified to the (130) plane of FeOOH. SEM imaging of the activated FeHCF electrode reveals the presence of intertwined nanowires forming a layer on the FeHCF electrode (Figure 1d). In contrast, the unactivated FeHCF electrode shows unchanged morphology after the first charge (Figure S6). The scanning transmission electron microscope high angle annular dark-field (STEM-HAADF) image of the formed nanowire exhibits the characteristics of polycrystalline consisting of nanograins (Figure 1e). The corresponding selected area electron diffraction (SAED) image indicates that the ring patterns align well with the (220), (321), and (660) planes of FeOOH (JCPDS 01-075-1594) (Figure 1f). The STEM-EELS elemental mapping (Figure 1g) shows a uniform distribution of Fe and O elements. Furthermore, quantitative element analysis of the red frame area indicates that the content of oxygen atoms is twice that of iron atoms (Figure 1h, Table S1). These results confirm that an intertwined nanowire layer composed of nanocrystalline FeOOH grains formed during the activation process. EDS-HAADF elemental mapping of the activated FeHCF electrode shows the well-dispersed FeOOH nanowire on the FeHCF particles, resulting in a structure of FeHCF particles tightly encapsulated by FeOOH nanowires (Figure 1i–n).

After 50 cycles, we opened a Fe/activated-FeHCF cell for post-mortem analysis and observed that the surface of the activated FeHCF is still covered with FeOOH nanowires as well as nanosheets that deposit in a flower-like arrangement as shown in Figure 2a and Figure S7. The size of the microflowers ranges from a few hundred nanometers to several micrometers (Figure 2b). High-resolution STEM-HAADF images of the microflower (Figure 2c) show well-defined lattice fringes with a *d*-spacing of 0.26 nm, which can be indexed to the (020) plane of crystalline $Fe_3(SO_4)_2(OH)_2$ (FSH) (JCPDS 96-411-9421). The SAED pattern of the microflower (Figure 2d) exhibits the diffraction rings indexed to (011), (013), (020), (121), (026), and (127) lattice planes of the FSH, confirming that the deposits formed after cycling are FSH. We hypothesize that these deposits are formed in a similar fashion to $Zn_4SO_4(OH)_6{\cdot}xH_2O$ observed in zinc ion batteries.[35−38]

https://doi.org/10.1021/acsnano.4c05561
ACS Nano 2024, 18, 17304−17313

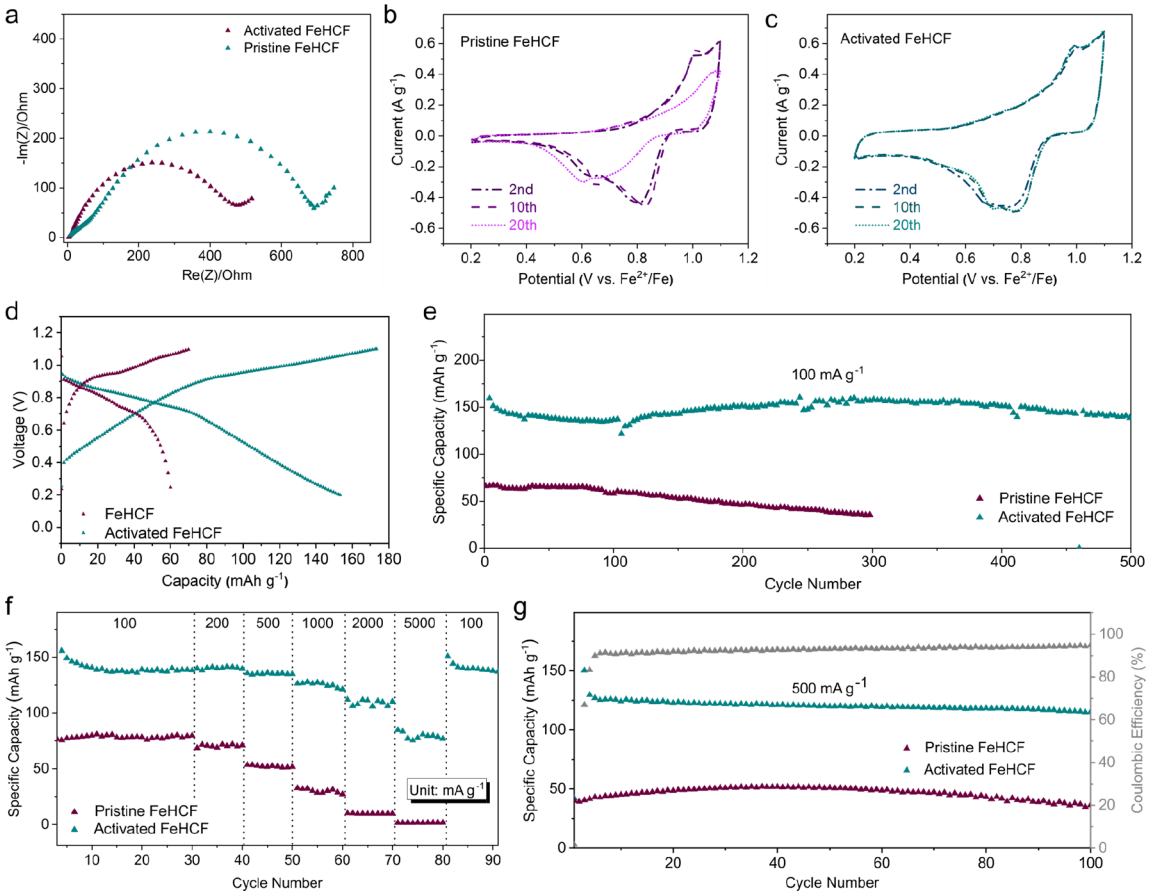

Figure 3. Electrochemical performance of pristine and activated FeHCF cathodes. (a) Nyquist impedance plots before and after activation. (b) Cyclic voltammograms (CV) curves of pristine FeHCF and (c) activated FeHCF at 0.5 mV s^{-1}. (d) Charge−discharge curves at 100 mA g^{-1}. (e) Long cycle performance at 100 mA g^{-1}. (f) Rate capability. (g) Cycling stability at 500 mA g^{-1}.

More specifically, as H^+ is inserted into the activated FeHCF, a hydroxide ion-rich layer develops near the electrode surface, leading to the formation of FSH microflowers according to the following equation:

$$3Fe^{2+} + 2SO_4^{2-} + 2OH^- \rightleftharpoons Fe_3(SO_4)_2(OH)_2 \quad (3)$$

Moreover, the FSH microflowers disappear after the subsequent charging process (see Figure S8). The reversible appearance and disappearance of FSH microflowers on the surface of the activated FeHCF cathode indicates reversible proton co-intercalation/deintercalation processes.[39] In comparison, the unactivated FeHCF electrode did not exhibit any microflowers on its surface after discharge (Figure S9). The notable contrast in surface appearances after discharging clearly indicates the distinct H^+ insertion behaviors between the activated FeHCF and unactivated FeHCF electrodes. The STEM image of the activated FeHCF at the discharge state after 50 cycles shows the coexistence of nanowires and microsheets on the surface (Figure 2e). The corresponding STEM-EELS spectra of the microsheet (area 1) and nanowire (area 2) demonstrate distinct Fe L-edges, as shown in Figure 2f. The Fe L_3-edge of the microsheet has a major peak at 708 eV, corresponding to a typical Fe^{II} valence state for FSH.[40,41] The FeOOH nanowire shows a Fe L_3-edge peak shifted by about 1 eV toward higher energy values, which agrees with the chemical shift rule that the Fe $L_{2,3}$-edge systematically shifts to higher energy losses for higher oxidation states, corresponding to the Fe^{III} for FeOOH.[42,43] EDS-HAADF elemental mapping (Figure 2g−k) images of the activated FeHCF electrode after cycling show that the FeOOH nanowires remain unchanged on the FeHCF particles. These results indicate that the FeOOH layer remains stable in morphology and valence state during the discharge process.

As discussed above, the activated FeHCF demonstrates enhanced H^+ intercalation compared to the unactivated FeHCF, while the FeOOH layer remains unchanged. Benefiting from the H^+ co-intercalation chemistry, the activated FeHCF exhibits notable improvements in electrochemical performance. Figure 3a shows the Nyquist plots of electrochemical impedance spectroscopy (EIS) for the unactivated FeHCF and activated FeHCF. The unactivated FeHCF exhibits a semicircle at high frequencies and a straight sloping line at low frequencies, corresponding to the charge transfer and Warburg diffusion, respectively.[44] After the activation process, FeHCF exhibits an additional semicircle at high frequency, which can account for the high surface FeOOH layer formation.[45,46] Cyclic voltammetry (CV) tests were employed to analyze the redox couples of FeHCF. The CV curves of pristine FeHCF (Figure 3b) show two cathodic peaks located at around 0.65 and 0.8 V; however, the response current of the peak at 0.65 V is weak. In contrast, the CV curves of activated FeHCF (Figure 3c) show two strong cathodic peaks located at around 0.8 and 0.7 V, demonstrating a two-step discharge of activated FeHCF. Moreover, the CV curves of activated FeHCF remain invariable during 20 cycles while the unactivated FeHCF fades rapidly, indicating much

https://doi.org/10.1021/acsnano.4c05561
ACS Nano 2024, 18, 17304−17313

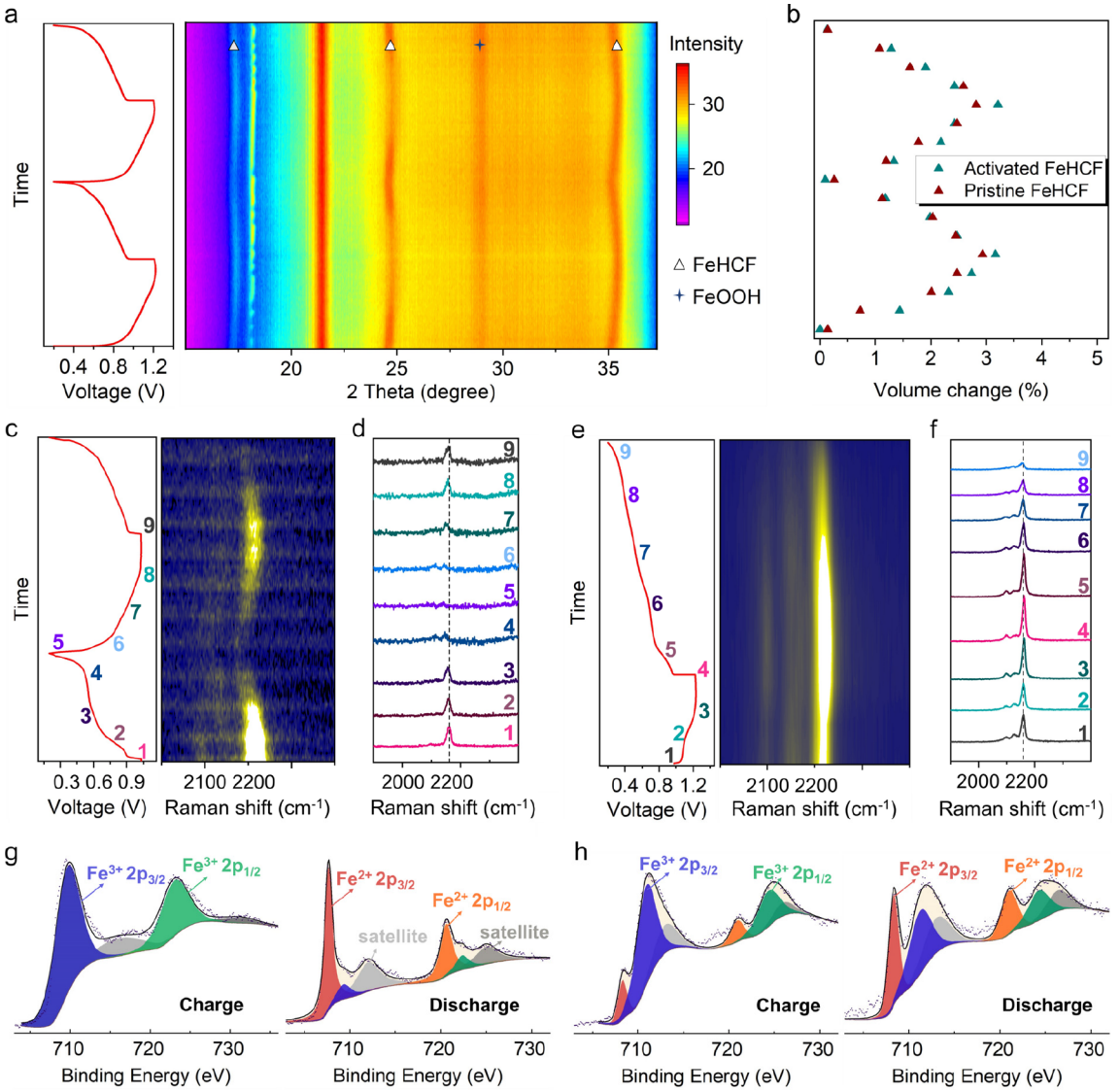

Figure 4. Structure and valence evolution of activated FeHCF cathode during charge and discharge processes. (a) In situ XRD characterization and the corresponding GCD voltage profiles of activated FeHCF during the first two charge/discharge cycles. (b) Lattice parameters during the first two charge/discharge cycles of both activated and pristine FeHCF. (c) In situ 2D Raman spectra and (d) the zoom-in Raman spectra at various points with corresponding GCD potential profiles of the activated FeHCF. (e) In situ 2D Raman spectra and (f) the zoom-in Raman spectra at various points with corresponding GCD potential profiles of the pristine FeHCF. (g) Fe 2p XPS spectra of activated FeHCF at full-discharged and full-charged states. (h) XPS spectra of pristine FeHCF at full-discharged and full-charged states.

better reversibility for H^+/Fe^{2+} co-intercalation/deintercalation. Consequently, the activated FeHCF shows a decent capacity of 151 mAh g^{-1} at 100 mA g^{-1}, which is 252% higher than that of the pristine FeHCF (60 mAh g^{-1}) (Figure 3d). This is the highest capacity reported for Prussian blue analogues (PBAs) cathodes in aqueous multivalent-ion battery systems including Fe-ion, Mg-ion, Ca-ion, and Al-ion batteries (Table S2). Figure 3e shows that the activated-FeHCF retains 93% of its capacity after 500 cycles. In contrast, the pristine FeHCF exhibits a lower initial discharge capacity of around 66 mAh g^{-1} and experiences continuous capacity fading over cycling. The increase in capacity observed in the activated FeHCF is well-maintained even at high charge/discharge rates (Figure 3f); for instance, at 5000 mA g^{-1}, a specific capacity of 77 mAh g^{-1} can still be sustained. When the current density decreases back to 100 mA g^{-1}, the discharge capacity of activated FeHCF returns to its original 150 mAh g^{-1} without visible degradation, with high rate stability demonstrated in Figure 3g. In contrast, the pristine FeHCF has hardly any capacity at 5000 mA g^{-1}.

To establish a comprehensive comparison, we substituted the FeHCF electrode with carbon paper (CP) and carbon cloth (CC) in the assembly of the Fe//CP and Fe//CC cells. Figure S10 shows the ex situ SEM images of CP and CC after a 16 h overcharging at 0.2 mAh cm^{-2}. The presence of intertwined nanowires growing on the surface of CP and CC demonstrates the formation of FeOOH films, similar to what was observed on FeHCF. We then conducted further testing of the electrochemical performance of the activated CP and CC electrodes. However, both electrodes exhibited almost negligible capacities, approximately 0.0025 mAh cm^{-2} (Figure S11). These results indicate that the FeOOH layer can be

https://doi.org/10.1021/acsnano.4c05561
ACS Nano 2024, 18, 17304−17313

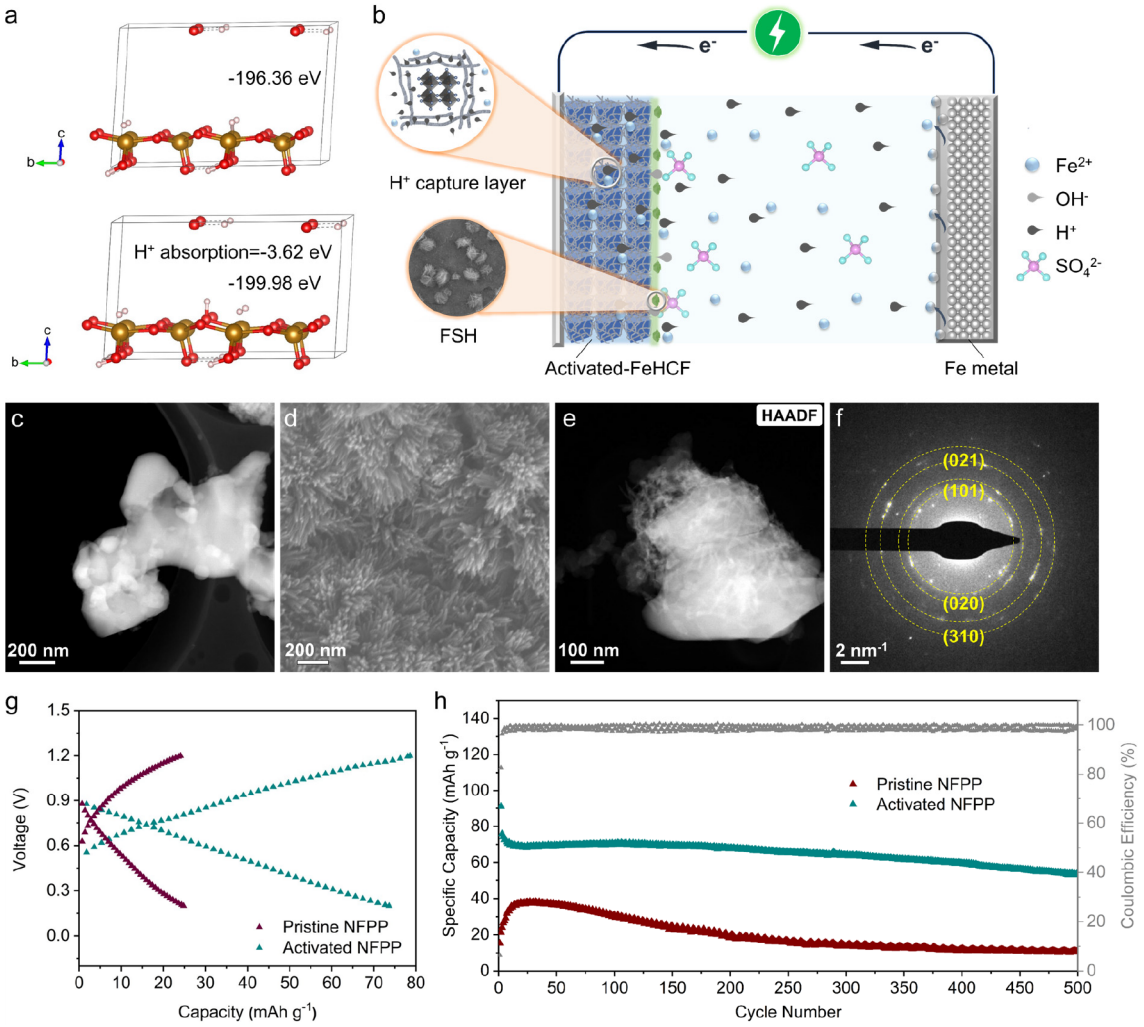

Figure 5. Extension of electrochemical activation to NFPP cathodes. (a) DFT calculation of the H^+ absorption effect of the FeOOH nanowire. (b) Schematic illustration of the discharge process of the activated cathode. (c) TEM image of synthesized NFPP. (d) SEM image of the surface of the activated NFPP electrode. (e) STEM-HAADF image of NFPP after activation. (f) SAED image of the activation product. (g) Charge−discharge curves of activated and pristine NFPP at 500 mA g^{-1}. (h) Cycle performance at 500 mA g^{-1}.

formed on various substrates after overcharging, but it does not directly contribute to the capacity of the battery. This finding is consistent with the previous observation that the valence state of FeOOH remains unchanged during the discharge process.

To investigate the crystal structure evolution of the activated FeHCF during electrochemical cycling, in situ XRD characterization was employed, as shown in Figure 4a. The diffraction peaks at around 17.5°, 24.8°, and 35.3° are identified to the (200), (220), and (400) lattice planes of FeHCF.[34] During the charging process, the diffraction planes of (220), (220), and (400) shift to higher angles, which means a decrease in lattice parameters due to the extraction of Fe^{2+}/H^+ ions. Conversely, these diffraction peaks shift back to lower angles during the following discharging process, indicating the intercalation of Fe^{2+}/H^+ ions. The peak shift is highly reversible in two electrochemical cycles, and the activated FeHCF maintains its face-centered cubic structure during the intercalation/deintercalation process. Moreover, the peak at 28° remains unchanged during the charge/discharge cycles, demonstrating the FeOOH layer does not involve the electrochemical reactions. The structural evolution observed in the pristine FeHCF electrode is nearly identical to that of the activated FeHCF electrode (Figure S12). The peaks corresponding to FeHCF shift toward a higher angle during charging and return to the original position after being fully discharged, while there is no peak at 28° appears. Figure 4b summarizes the lattice parameters of both activated and pristine FeHCF during charge and discharge. The isotropic lattice contraction of activated FeHCF reaches 1.07% (10.205−10.096 Å) during charge, the lattice expansion reaches 1.04% (10.096 to 10.202 Å) during discharge, and the total volume change calculated is 3.16% (1062.7−1029.1 $Å^3$). By comparison, the pristine FeHCF exhibits a similar volume change of 2.93% during cycling, even though its specific capacity is less than half of the activated FeHCF. This is attributed to the proton insertion having minimal impact on the lattice parameters in FeHCF.[18]

In situ Raman and ex situ XPS tests were conducted to investigate the redox evolution during charge/discharge. Figure 4c shows the Raman spectra of activated FeHCF during the first two cycles. During discharging, the Fe^{3+}-coordinated ν(CN) band (2150 cm^{-1})[47,48] of activated FeHCF has a red shift and its intensity simultaneously fades. Figure 4d demonstrates the absence of a Raman signal at 2150 cm^{-1} in the fully discharged state, suggesting the successful reduction

https://doi.org/10.1021/acsnano.4c05561
ACS Nano 2024, 18, 17304−17313

of almost all of the Fe^{3+} in activated FeHCF to Fe^{2+}. The bond variation during charging is an inverse process; the peak at 2150 cm^{-1} blue shifts back to the higher position, and it is highly reversible. In the case of pristine FeHCF, the Fe^{3+}-coordinated ν(CN) band shows a minimal peak shift during the electrochemical process. While its intensity diminishes with discharge, it still exists in the fully discharged state (Figure 4e,f). This result indicates that only a portion of trivalent iron in pristine FeHCF can be reduced during discharging, leading to a limited specific capacity.

Ex situ XPS further confirms the difference in the oxidation states between activated FeHCF and pristine FeHCF during the electrochemical charge/discharge processes. Figure 4g presents the Fe 2p XPS spectra for activated FeHCF, the peaks at 707.7 and 720.8 eV are assigned to Fe^{II} 2p3/2 and Fe^{II} 2p1/2, respectively, while the peaks at 710 and 722.8 eV are attributed to Fe^{III} 2p3/2 and Fe^{III} 2p1/2, respectively.[33,49] At a fully charged state, almost all of the Fe^{II} in activated FeHCF is oxidized to Fe^{III}. After being fully discharged, the area ratio of the Fe^{II} peaks increases, indicating an average valence value decreased from 2.95 to 2.14 (corresponding to a specific capacity of 149.1 mAh g^{-1}). In comparison, pristine FeHCF retains a high proportion of trivalent iron after being fully discharged (Figure 4h). The average valence value of pristine FeHCF decreased from 2.84 to 2.48, corresponding to a specific capacity of 61.2 mAh g^{-1}. These results align with the electrochemical performance discussed above.

Based on the discussions above regarding electrochemistry and characterization, we further conducted DFT calculations that revealed the proton capture effect of the FeOOH layer. The FeOOH exhibits a low H^+ absorption energy of −3.62 eV per unit, which is much lower than that of FeHCF (Figures 5a and S13). As illustrated in Figure 5b, during discharging the high surface area and low H^+ absorption energy of the FeOOH nanowire layer serve as a proton trapper on the surface of the activated-FeHCF cathode, accelerating proton intercalation. Consequently, the insertion of protons results in the formation of FHS microflowers as we discussed in Figure 2.

To explore the applicability of this activation process in other AIIBs, we assembled an AIIB with NFPP as the cathode material. NFPP was synthesized using a simple solid-state method, resulting in irregular particle shapes (Figure 5c and Figure S14). The XRD pattern of the NFPP cathode matches well with the previously reported NFPP[50] (Figure S15). EDS-HAADF elemental mappings of the NFPP reveal a homogeneous distribution of Na, Fe, O, and P elementals (Figure S16). As shown in Figure S17, the FT-IR spectrum of the NFPP exhibits peaks in the ranges of 450−650 cm^{-1} and 975−1200 cm^{-1}, corresponding to vibrations in PO_4 groups, while the peaks at 719 and 956 cm^{-1} align with the vibrations in P_2O_7 groups.[51,52] Interestingly, similar to the activated FeHCF, the activation process also results in intertwined nanowires that are uniformly distributed on the NFPP particles (Figure 5d,e). The SAED pattern of the nanowires aligns well with the (101), (020), (021), and (310) planes of FeOOH (Figure 5f). These results demonstrate the successful extension of the activation process to the Fe//NFPP battery, resulting in a FeOOH nanowire-coated NFPP cathode.

Similar to the FeHCF cathode, the activated-NFPP exhibits a more than 2-fold capacity compared with pristine NFPP in the AIIB system (Figure 5g). As shown in Figure 5h, the activated NFPP delivers a stable capacity of around 70 mAh g^{-1} over 500 cycles, with an average Coulombic efficiency of 100%. In contrast, pristine NFPP exhibits a much lower capacity of 35 mAh g^{-1} and experiences significant fading, reaching only 17 mAh g^{-1} after 200 cycles. Moreover, the activated NFPP cathode demonstrates enhanced rate capacities compared to the pristine NFPP due to the beneficial proton co-intercalation (Figure S18). In situ XRD characterization was conducted to reveal the reaction mechanism of the activated NFPP cathode. During the charging process, peaks at 23.9°, 25.8°, 28.6°, 32.1°, 32.7°, and 33.6°, correspond to (410), (402), (013), (022), (610), and (004) lattice planes of NFPP, shift to higher angles, demonstrating the lattice shrinks due to Fe^{2+}/H^+ deintercalation (see Figure S19). During the subsequent discharge, these peaks shift back to lower angles due to Fe^{2+}/H^+ insertion. This highly reversible lattice shrinkage−expansion process indicates reversible insertion−extraction reactions during electrochemical cycling in the activated NFPP cathode. These results demonstrate that the activation process is feasible for extension to other cathode materials, leading to an enhancement in the material capacity and cycling performance.

3. CONCLUSION

In summary, we have developed an electrochemical activation process for AIIB cathodes, which doubles their capacity and improves the rate performance and cyclability. We show that this is because this process facilitates H^+ co-intercalation. The in situ formed FeOOH nanowires during activation act as a proton capture layer, enhancing H^+ insertion in cathode materials. This mechanism contributes to the substantial improvements in the electrochemical performance of the activated cathodes in AIIBs. We have demonstrated that this process is applicable to two different cathode materials both showing a doubling in specific capacity and cycling performance by introducing proton co-insertion. The activated FeHCF cathode exhibits a capacity of 151 mAh g^{-1} at 100 mA g^{-1}, surpassing all previously reported Prussian blue analogues used as cathodes in aqueous multivalent-ion batteries. These findings highlight the potential of the activation process to make AIIBs suitable for real life applications, for instance, to store renewable energy sources.

4. METHODS

4.1. Preparation of FeHCF Cathode. FeHCF was prepared by a mature co-precipitation method with slight modification. Solution A: 5 mmol of $FeSO_4$ and 10 mmol of HCl were dissolved in 100 mL of deionized water. Solution B: 2.5 mmol of $K_4Fe(CN)_6$ was dissolved in 100 mL of deionized water. Solution A was added into solution B drop by drop under vigorous stirring in a water bath at 60 °C, and then the mixture was held at temperature for 2 h to complete the coordination reaction. Then, the mixed solution was aged at room temperature for 12 h. After that, the product was isolated by centrifugation and washed with deionized water four times. Finally, FeHCF powder was obtained after being dried in an oven at 80 °C for 24 h.

4.2. Preparation of NFPP Cathode. NFPP was synthesized by using a solid-state method. Typically, 1 mmol of $Na_4P_2O_7{\cdot}10H_2O$ (≥99.0%, AR), 3 mmol of $FeSO_4{\cdot}7H_2O$ (≥99.0%, AR), and 2 mmol of $NH_4H_2PO_4$ (≥99.0%, AR) were mixed in deionized water. Besides, 4.5 mmol of citric acid (≥99.5%, AR) was added into the mixture to integrate carbon with NFPP to improve its electronic conductivity. The obtained mixture was then dried at 140 °C for 12 h, and the NFPP was obtained after the homogeneous mixed powder was heated at 500 °C (5 °C min^{-1}) in vacuum condition for 10 h.

4.3. Materials Characterization. The phase of the obtained FeHCF was characterized by an X-ray diffractometer (Bruker D2

https://doi.org/10.1021/acsnano.4c05561
ACS Nano 2024, 18, 17304−17313

Phaser, Cu Kα radiation). The morphology of the samples was observed using a field-emission scanning electron microscope (SEM, JEOL JSM-7100F). Transmission electron microscope (TEM) images, high angle annular dark field imaging-scanning TEM (HAADF-STEM), selected area electron diffraction (SAED) patterns, elemental mappings, and electron energy loss spectroscopy (EELS) spectra of the samples were characterized by a double spherical aberration corrected transmission electron microscope (Titan Cubed Themis G2 300/Titan Cubed Themis G2 30). Fourier transform infrared (FT-IR) transmittance spectra and in situ/ex situ Raman spectra were acquired using a Nicolet 6700 (Thermo Fisher Scientific Co., USA) IR spectrometer and HORIBA HR EVO Raman system with an excitation laser of 633 nm, respectively. Ex situ X-ray photoelectron spectroscopy (XPS) spectra were recorded by using a PerkinElmer Optima 4300DV spectrometer.

4.4. In Situ Electrochemistry-XRD/Raman Tests. The in situ batteries for XRD and Raman testing were assembled by using mold cells, with cling film and sapphire serving as the windows, respectively. In situ electrochemistry-XRD tests were carried out using a Bruker D8 Advance X-ray diffractometer (Cu Kα radiation, λ= 1.5418 Å) and a Land battery test system (LAND CT2001A). The in situ XRD singles were collected by the planar detector in a still mode during the charge−discharge processes; each pattern took 110 s. In situ electrochemistry-Raman measurements were conducted by using a HORIBA HREVO Raman system (633 nm laser) and a Land battery test system (LAND CT2001A), and the Raman spectra were recorded with a time interval of 200 s.

ASSOCIATED CONTENT

Supporting Information

The Supporting Information is available free of charge at https://pubs.acs.org/doi/10.1021/acsnano.4c05561.

Experimental procedures including electrochemical measurements and DFT calculations method; additional materials synthesis, characterization, and electrochemical data (PDF)

AUTHOR INFORMATION

Corresponding Authors

Michael F. L. De Volder − *Institute for Manufacturing, Department of Engineering, University of Cambridge, Cambridge CB3 0FS, U.K.*; Email: mfld2@cam.ac.uk

Qinyou An − *Key Laboratory of Advanced Technology for Materials Synthesis and Processing, Wuhan University of Technology, Wuhan 430070, China; Hubei Longzhong Laboratory, Xiangyang Demonstration Zone, Wuhan University of Technology, Xiangyang 441000 Hubei, China*; orcid.org/0000-0003-0605-4942; Email: anqinyou86@whut.edu.cn

Liqiang Mai − *Key Laboratory of Advanced Technology for Materials Synthesis and Processing, Wuhan University of Technology, Wuhan 430070, China; Hubei Longzhong Laboratory, Xiangyang Demonstration Zone, Wuhan University of Technology, Xiangyang 441000 Hubei, China*; Email: mlq518@whut.edu.cn

Authors

Ze He − *Key Laboratory of Advanced Technology for Materials Synthesis and Processing, Wuhan University of Technology, Wuhan 430070, China; Institute for Manufacturing, Department of Engineering, University of Cambridge, Cambridge CB3 0FS, U.K.*

Gao Wang − *Key Laboratory of Advanced Technology for Materials Synthesis and Processing, Wuhan University of Technology, Wuhan 430070, China*

Ruohan Yu − *Key Laboratory of Advanced Technology for Materials Synthesis and Processing, Wuhan University of Technology, Wuhan 430070, China*

Yalong Jiang − *State Key Laboratory of New Textile Materials and Advanced Processing Technologies, Wuhan Textile University, Wuhan 430200, China*

Meng Huang − *Sanya Science and Education Innovation Park of Wuhan University of Technology, Sanya 572000, China*

Fangyu Xiong − *College of Materials Science and Engineering, Chongqing University, Chongqing 400030, China*

Shuangshuang Tan − *College of Materials Science and Engineering, Chongqing University, Chongqing 400030, China*; orcid.org/0009-0000-4957-1566

Complete contact information is available at: https://pubs.acs.org/10.1021/acsnano.4c05561

Author Contributions

The manuscript was written through contributions of all authors. All authors have given approval to the final version of the manuscript.

Notes

The authors declare no competing financial interest.

ACKNOWLEDGMENTS

This work was supported by the National Key Research and Development Program of China (Grants 2020YFA0715000 and 2023YFB3809800), National Energy-Saving and Low-Carbon Materials Production and Application Demonstration Platform Program (Grant TC220H06N), National Natural Science Foundation of China (Grant 52127816), Natural Science Foundation of Hubei Province (Grant 2022CFA087), Hainan Provincial Joint Project of Sanya Yazhou Bay Science and Technology City (Grant 2021CXLH0007), and ERC Consolidator Grant 866005-MIGHTY.

REFERENCES

(1) Chen, S.; Xia, Y.; Zeng, R.; Luo, Z.; Wu, X.; Hu, X.; Lu, J.; Gazit, E.; Pan, H.; Hong, Z.; Yan, M.; Tao, K.; Jiang, Y. Ordered Planar Plating/Stripping Enables Deep Cycling Zinc Metal Batteries. *Sci. Adv.* **2024**, *10*, eadn2265.

(2) Jin, S.; Shao, Y.; Gao, X.; Chen, P.; Zheng, J.; Hong, S.; Yin, J.; Joo, Y. L.; Archer, L. A. Designing Interphases for Practical Aqueous Zinc Flow Batteries with High Power Density and High Areal Capacity. *Sci. Adv.* **2022**, *8*, eabq4456.

(3) Zheng, J.; Archer, L. A. Controlling Electrochemical Growth of Metallic Zinc Electrodes: Toward Affordable Rechargeable Energy Storage Systems. *Sci. Adv.* **2021**, *7*, eabe0219.

(4) Zhang, N.; Chen, X.; Yu, M.; Niu, Z.; Cheng, F.; Chen, J. Materials Chemistry for Rechargeable Zinc-Ion Batteries. *Chem. Soc. Rev.* **2020**, *49*, 4203−4219.

(5) Zheng, J.; Zhao, Q.; Tang, T.; Yin, J.; Quilty, C. D.; Renderos, G. D.; Liu, X.; Deng, Y.; Wang, L.; Bock, D. C.; Jaye, C.; Zhang, D.; Takeuchi, E. S.; Takeuchi, K. J.; Marschilok, A. C.; Archer, L. A. Reversible Epitaxial Electrodeposition of Metals in Battery Anodes. *Science* **2019**, *366*, 645−648.

(6) Wu, X.; Markir, A.; Xu, Y.; Zhang, C.; Leonard, D. P.; Shin, W.; Ji, X. A Rechargeable Battery with an Iron Metal Anode. *Adv. Funct. Mater.* **2019**, *29*, 1900911.

(7) He, Z.; Xiong, F.; Tan, S.; Yao, X.; Zhang, C.; An, Q. Iron Metal Anode for Aqueous Rechargeable Batteries. *Mater. Today Adv.* **2021**, *11*, 100156.

(8) Xu, X.; Chao, D.; Chen, B.; Liang, P.; Li, H.; Xie, F.; Davey, K.; Qiao, S.-Z. Revealing the Magnesium-Storage Mechanism in Mesoporous Bismuth via Spectroscopy and Ab-Initio Simulations. *Angew. Chem., Int. Ed.* **2020**, *59*, 21728−21735.

(9) Xu, X.; Ye, C.; Chao, D.; Chen, B.; Li, H.; Tang, C.; Zhong, X.; Qiao, S.-Z. Synchrotron X-Ray Spectroscopic Investigations of In-Situ-Formed Alloy Anodes for Magnesium Batteries. *Adv. Mater.* **2022**, *34*, 2108688.
(10) Wu, X.; Markir, A.; Xu, Y.; Hu, E. C.; Dai, K. T.; Zhang, C.; Shin, W.; Leonard, D. P.; Kim, K.; Ji, X. Rechargeable Iron−Sulfur Battery without Polysulfide Shuttling. *Adv. Energy Mater.* **2019**, *9*, 1902422.
(11) Bai, C.; Jin, H.; Gong, Z.; Liu, X.; Yuan, Z. A High-Power Aqueous Rechargeable Fe-I2 Battery. *Energy Storage Mater.* **2020**, *28*, 247−254.
(12) Saroja, A. P. V. K.; Smruti Samantaray, S.; Sundara, R. A Room Temperature Multivalent Rechargeable Iron Ion Battery with an Ether Based Electrolyte: A New Type of Post-Lithium Ion Battery. *Chem. Commun.* **2019**, *55*, 10416−10419.
(13) Xu, Y.; Wu, X.; Sandstrom, S. K.; Hong, J. J.; Jiang, H.; Chen, X.; Ji, X. Fe-Ion Bolted VOPO4·2H2O as an Aqueous Fe-Ion Battery Electrode. *Adv. Mater.* **2021**, *33*, 2105234.
(14) Lv, H.; Wei, Z.; Han, C.; Yang, X.; Tang, Z.; Zhang, Y.; Zhi, C.; Li, H. Cross-Linked Polyaniline for Production of Long Lifespan Aqueous Iron||organic Batteries with Electrochromic Properties. *Nat. Commun.* **2023**, *14*, 3117.
(15) Wan, F.; Zhang, L.; Dai, X.; Wang, X.; Niu, Z.; Chen, J. Aqueous Rechargeable Zinc/Sodium Vanadate Batteries with Enhanced Performance from Simultaneous Insertion of Dual Carriers. *Nat. Commun.* **2018**, *9*, 1656.
(16) Wang, S.; Yuan, Z.; Zhang, X.; Bi, S.; Zhou, Z.; Tian, J.; Zhang, Q.; Niu, Z. Non-Metal Ion Co-Insertion Chemistry in Aqueous Zn/MnO2 Batteries. *Angew. Chem.* **2021**, *133*, 7132−7136.
(17) Gao, X.; Wu, H.; Li, W.; Tian, Y.; Zhang, Y.; Wu, H.; Yang, L.; Zou, G.; Hou, H.; Ji, X. H+-Insertion Boosted α-MnO2 for an Aqueous Zn-Ion Battery. *Small* **2020**, *16*, 1905842.
(18) Wu, X.; Hong, J. J.; Shin, W.; Ma, L.; Liu, T.; Bi, X.; Yuan, Y.; Qi, Y.; Surta, T. W.; Huang, W.; Neuefeind, J.; Wu, T.; Greaney, P. A.; Lu, J.; Ji, X. Diffusion-Free Grotthuss Topochemistry for High-Rate and Long-Life Proton Batteries. *Nat. Energy* **2019**, *4*, 123−130.
(19) Tie, Z.; Liu, L.; Deng, S.; Zhao, D.; Niu, Z. Proton Insertion Chemistry of a Zinc−Organic Battery. *Angew. Chem.* **2020**, *132*, 4950−4954.
(20) Wang, X.; Xie, Y.; Tang, K.; Wang, C.; Yan, C. Redox Chemistry of Molybdenum Trioxide for Ultrafast Hydrogen-Ion Storage. *Angew. Chem., Int. Ed.* **2018**, *57*, 11569−11573.
(21) Zhu, K.; Wu, T.; Sun, S.; van den Bergh, W.; Stefik, M.; Huang, K. Synergistic H+/Zn2+ Dual Ion Insertion Mechanism in High-Capacity and Ultra-Stable Hydrated VO2 Cathode for Aqueous Zn-Ion Batteries. *Energy Storage Mater.* **2020**, *29*, 60−70.
(22) Zhao, Q.; Chen, X.; Wang, Z.; Yang, L.; Qin, R.; Yang, J.; Song, Y.; Ding, S.; Weng, M.; Huang, W.; Liu, J.; Zhao, W.; Qian, G.; Yang, K.; Cui, Y.; Chen, H.; Pan, F. Unravelling H+/Zn2+ Synergistic Intercalation in a Novel Phase of Manganese Oxide for High-Performance Aqueous Rechargeable Battery. *Small* **2019**, *15*, 1904545.
(23) Liang, G.; Mo, F.; Ji, X.; Zhi, C. Non-Metallic Charge Carriers for Aqueous Batteries. *Nat. Rev. Mater.* **2021**, *6*, 109−123.
(24) Sun, W.; Wang, F.; Hou, S.; Yang, C.; Fan, X.; Ma, Z.; Gao, T.; Han, F.; Hu, R.; Zhu, M.; Wang, C. Zn/MnO2 Battery Chemistry With H+ and Zn2+ Coinsertion. *J. Am. Chem. Soc.* **2017**, *139*, 9775−9778.
(25) Zhao, Q.; Song, A.; Zhao, W.; Qin, R.; Ding, S.; Chen, X.; Song, Y.; Yang, L.; Lin, H.; Li, S.; Pan, F. Boosting the Energy Density of Aqueous Batteries via Facile Grotthuss Proton Transport. *Angew. Chem.* **2021**, *133*, 4215−4220.
(26) Jin, Y.; Zou, L.; Liu, L.; Engelhard, M. H.; Patel, R. L.; Nie, Z.; Han, K. S.; Shao, Y.; Wang, C.; Zhu, J.; Pan, H.; Liu, J. Joint Charge Storage for High-Rate Aqueous Zinc−Manganese Dioxide Batteries. *Adv. Mater.* **2019**, *31*, 1900567.
(27) Bin, D.; Wang, F.; Tamirat, A. G.; Suo, L.; Wang, Y.; Wang, C.; Xia, Y. Progress in Aqueous Rechargeable Sodium-Ion Batteries. *Adv. Energy Mater.* **2018**, *8*, 1703008.
(28) Qiao, J.; Liu, Z.; Wang, Z.; Qin, M.; Shi, Y.; Xu, J.; Chen, Z.; Cao, J. Long-Life Aqueous H+/K+ Dual-Cation Batteries Based on Dipyridophenazine//Hexacyanoferrate Electrodes. *ACS Appl. Energy Mater.* **2021**, *4*, 4903−4909.
(29) Jia, X.; Liu, C.; Neale, Z. G.; Yang, J.; Cao, G. Active Materials for Aqueous Zinc Ion Batteries: Synthesis, Crystal Structure, Morphology, and Electrochemistry. *Chem. Rev.* **2020**, *120*, 7795−7866.
(30) Huang, W.; Zhang, K.; Yuan, B.; Yang, L.; Zhu, M. Predominant Intercalation of H+ Enables Ultrahigh Rate Capability of Oxygen Deficient MoO3 for Aqueous Al-Ion Batteries. *Energy Storage Mater.* **2022**, *50*, 152−160.
(31) Zhao, Q.; Liu, L.; Yin, J.; Zheng, J.; Zhang, D.; Chen, J.; Archer, L. A. Proton Intercalation/De-Intercalation Dynamics in Vanadium Oxides for Aqueous Aluminum Electrochemical Cells. *Angew. Chem., Int. Ed.* **2020**, *59*, 3048−3052.
(32) Yang, C.; Pu, Z.; Jiang, Z.; Gao, X.; Wang, K.; Wang, S.; Chai, Y.; Li, Q.; Wu, X.; Xiao, Y.; Xu, D. H2O-Boosted Mg−Proton Collaborated Energy Storage for Rechargeable Mg-Metal Batteries. *Adv. Energy Mater.* **2022**, *12*, 2201718.
(33) He, X.; Tian, L.; Qiao, M.; Zhang, J.; Geng, W.; Zhang, Q. A Novel Highly Crystalline Fe 4 (Fe(CN) 6) 3 Concave Cube Anode Material for Li-Ion Batteries with High Capacity and Long Life. *J. Mater. Chem. A* **2019**, *7*, 11478−11486.
(34) Yang, Q.; Mo, F.; Liu, Z.; Ma, L.; Li, X.; Fang, D.; Chen, S.; Zhang, S.; Zhi, C. Activating C-Coordinated Iron of Iron Hexacyanoferrate for Zn Hybrid-Ion Batteries with 10 000-Cycle Lifespan and Superior Rate Capability. *Adv. Mater.* **2019**, *31*, 1901521.
(35) Pan, H.; Shao, Y.; Yan, P.; Cheng, Y.; Han, K. S.; Nie, Z.; Wang, C.; Yang, J.; Li, X.; Bhattacharya, P.; Mueller, K. T.; Liu, J. Reversible Aqueous Zinc/Manganese Oxide Energy Storage from Conversion Reactions. *Nat. Energy* **2016**, *1*, 16039.
(36) Huang, J.; Wang, Z.; Hou, M.; Dong, X.; Liu, Y.; Wang, Y.; Xia, Y. Polyaniline-Intercalated Manganese Dioxide Nanolayers as a High-Performance Cathode Material for an Aqueous Zinc-Ion Battery. *Nat. Commun.* **2018**, *9*, 2906.
(37) Yuan, Y.; Sharpe, R.; He, K.; Li, C.; Saray, M. T.; Liu, T.; Yao, W.; Cheng, M.; Jin, H.; Wang, S.; Amine, K.; Shahbazian-Yassar, R.; Islam, M. S.; Lu, J. Understanding Intercalation Chemistry for Sustainable Aqueous Zinc−Manganese Dioxide Batteries. *Nat. Sustain.* **2022**, *5*, 890−898.
(38) Wang, J.; Wang, J.-G.; Liu, H.; Wei, C.; Kang, F. Zinc Ion Stabilized MnO 2 Nanospheres for High Capacity and Long Lifespan Aqueous Zinc-Ion Batteries. *J. Mater. Chem. A* **2019**, *7*, 13727−13735.
(39) He, Q.; Hu, T.; Wu, Q.; Wang, C.; Han, X.; Chen, Z.; Zhu, Y.; Chen, J.; Zhang, Y.; Shi, L.; Wang, X.; Ma, Y.; Zhao, J. Tunnel-Oriented VO2 (B) Cathode for High-Rate Aqueous Zinc-Ion Batteries. *Adv. Mater.* **2024**, 2400888.
(40) He, K.; Zhou, Y.; Gao, P.; Wang, L.; Pereira, N.; Amatucci, G. G.; Nam, K.-W.; Yang, X.-Q.; Zhu, Y.; Wang, F.; Su, D. Sodiation via Heterogeneous Disproportionation in FeF2 Electrodes for Sodium-Ion Batteries. *ACS Nano* **2014**, *8*, 7251−7259.
(41) Garvie, L. A. J.; Buseck, P. R. Ratios of Ferrous to Ferric Iron from Nanometre-Sized Areas in Minerals. *Nature* **1998**, *396*, 667−670.
(42) Tan, H.; Verbeeck, J.; Abakumov, A.; Van Tendeloo, G. Oxidation State and Chemical Shift Investigation in Transition Metal Oxides by EELS. *Ultramicroscopy* **2012**, *116*, 24−33.
(43) Schmid, H. K.; Mader, W. Oxidation States of Mn and Fe in Various Compound Oxide Systems. *Micron* **2006**, *37*, 426−432.
(44) Thomas, M. G. S. R.; Bruce, P. G.; Goodenough, J. B. AC Impedance Analysis of Polycrystalline Insertion Electrodes: Application to Li1−x CoO2. *J. Electrochem. Soc.* **1985**, *132*, 1521.
(45) Asakura, R.; Reber, D.; Duchêne, L.; Payandeh, S.; Remhof, A.; Hagemann, H.; Battaglia, C. 4 V Room-Temperature All-Solid-State Sodium Battery Enabled by a Passivating Cathode/Hydroborate Solid Electrolyte Interface. *Energy Environ. Sci.* **2020**, *13*, 5048−5058.

https://doi.org/10.1021/acsnano.4c05561
ACS Nano 2024, 18, 17304−17313

(46) Han, S.-D.; Kim, S.; Li, D.; Petkov, V.; Yoo, H. D.; Phillips, P. J.; Wang, H.; Kim, J. J.; More, K. L.; Key, B.; Klie, R. F.; Cabana, J.; Stamenkovic, V. R.; Fister, T. T.; Markovic, N. M.; Burrell, A. K.; Tepavcevic, S.; Vaughey, J. T. Mechanism of Zn Insertion into Nanostructured δ-MnO2: A Nonaqueous Rechargeable Zn Metal Battery. *Chem. Mater.* **2017**, *29*, 4874−4884.
(47) Samain, L.; Gilbert, B.; Grandjean, F.; Long, G. J.; Strivay, D. Redox Reactions in Prussian Blue Containing Paint Layers as a Result of Light Exposure. *J. Anal. At. Spectrom.* **2013**, *28*, 524−535.
(48) Xie, B.; Zuo, P.; Wang, L.; Wang, J.; Huo, H.; He, M.; Shu, J.; Li, H.; Lou, S.; Yin, G. Achieving Long-Life Prussian Blue Analogue Cathode for Na-Ion Batteries via Triple-Cation Lattice Substitution and Coordinated Water Capture. *Nano Energy* **2019**, *61*, 201−210.
(49) Wang, H.; Wang, L.; Chen, S.; Li, G.; Quan, J.; Xu, E.; Song, L.; Jiang, Y. Crystallographic-Plane Tuned Prussian-Blue Wrapped with RGO: A High-Capacity, Long-Life Cathode for Sodium-Ion Batteries. *J. Mater. Chem. A* **2017**, *5*, 3569−3577.
(50) Kim, H.; Park, I.; Seo, D.-H.; Lee, S.; Kim, S.-W.; Kwon, W. J.; Park, Y.-U.; Kim, C. S.; Jeon, S.; Kang, K. New Iron-Based Mixed-Polyanion Cathodes for Lithium and Sodium Rechargeable Batteries: Combined First Principles Calculations and Experimental Study. *J. Am. Chem. Soc.* **2012**, *134*, 10369−10372.
(51) Yuan, T.; Wang, Y.; Zhang, J.; Pu, X.; Ai, X.; Chen, Z.; Yang, H.; Cao, Y. 3D Graphene Decorated Na4Fe3(PO4)2(P2O7) Microspheres as Low-Cost and High-Performance Cathode Materials for Sodium-Ion Batteries. *Nano Energy* **2019**, *56*, 160−168.
(52) Xiong, F.; Li, J.; Zuo, C.; Zhang, X.; Tan, S.; Jiang, Y.; An, Q.; Chu, P. K.; Mai, L. Mg-Doped Na4Fe3(PO4)2(P2O7)/C Composite with Enhanced Intercalation Pseudocapacitance for Ultra-Stable and High-Rate Sodium-Ion Storage. *Adv. Funct. Mater.* **2023**, *33*, 2211257.

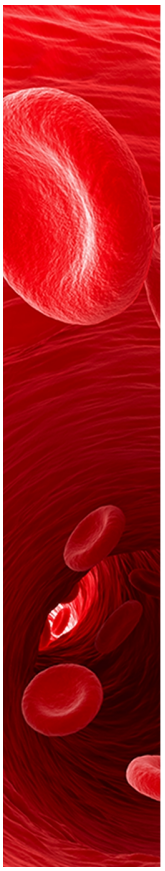
CAS BIOFINDER DISCOVERY PLATFORM™
CAS BIOFINDER HELPS YOU FIND YOUR NEXT BREAKTHROUGH FASTER
Navigate pathways, targets, and diseases with precision
Explore CAS BioFinder
CAS
A division of the American Chemical Society

https://doi.org/10.1021/acsnano.4c05561
ACS Nano 2024, 18, 17304−17313